An Alternative Approach to Contact-Based CubeSat-Pod Structural Interface

Esat Ulusoy [1], Semih Öztürk [1], Galip Orkun Arıcan [1,*]

Abstract

This study presents the dynamic behaviour of a 3U CubeSat structure under launch conditions, proposing an alternative boundary condition to bring test and finite element analysis (FEA) results closer together. The assumptions of bottom fixation, bottom-top fixation and rail fixation seen in the literature can represent the real system as being either too soft or too rigid, potentially making designs either overly conservative or overly optimistic. With this motivation, the CubeSat–pod interface was modelled with 6-degree-of-freedom spring (CBUSH) stiffnesses derived from Hertz–Mindlin–Popov contact theories. The proposed approach was verified with a part-to-whole strategy: (i) Printed Circuit Board (PCB)-standoff set (test 360 Hz, analysis 365 Hz; 1.4% difference), (ii) PCB-standoff-dummy mass set (test 246 Hz, analysis 250 Hz; 1.6% difference), and (iii) whole CubeSat was applied test and analysis for different boundary conditions. For proposed boundary condition, the analysis results were 96/126 Hz along the lateral axes, the test results were 96.7/120 Hz; along the longitudinal axis, test and analysis results were 137.9 Hz and 138 Hz, respectively. The test-analysis difference was minimum 14.7% with common boundary conditions in the literature, whereas a maximum deviation of 4.7% was observed with the proposed contact-based boundary condition, which yields an enhancement of better than 10% in natural frequency predictions. The results indicate that the analyses performed using the proposed boundary condition show a high level of agreement with the actual test data. Based on this finding, the proposed approach can lead to low-cost and time-effective satellite testing and design processes.

Keywords: CubeSat, contact theory, finite element method, modal analysis, boundary condition.

Received: 07.11.2025 Accepted: 22.12.2025 Research Article

[1] Aselsan Inc., Ankara, Türkiye
* Corresponding author.
✉ goarican@aselsan.com

Cite this article as: Ulusoy, E., Öztürk S., & Arıcan, G. O. (2026). An alternative approach to contact-based CubeSat-pod structural interface. *Journal of Defence and Security Industry: Strategy and Technology 1*, 71-95.

1. Introduction

With the rapid developments in space industry have led to a growing significance of small satellites, particularly CubeSats. By reason of their standardized structures, low costs, and limited time periods, CubeSats are widely used in both civilian and tactical fields, undertaking a wide range of tasks from communication to observation, data transmission to defence and security applications (Areda et al., 2022; Bomani et al., 2021). In an era where even a simple household appliance can exchange data remotely, CubeSats have become a fundamental component of the space-based Internet of Things (IoT) ecosystem. The flexibility they offer, particularly in areas such as surveillance, intelligence, signal tracking, and rapid communication, makes them a strategic asset in defence and security.

The great augmentation in the number of CubeSats has emerged a need for low-cost and easy-of-manufacture solutions. In this context, it is crucial to develop systems that are robust and optimized to meet mission requirements, rather than over-designed or over-qualified products in both design and testing processes (Kanavouras et al., 2022). In this regard, the use of more accurate modelling techniques and verified analysis methods enables shorter testing times and lower development costs. Thus, a sustainable engineering approach in space systems can be achieved without compromising reliability and while increasing production efficiency (Kempf et al., 2021).

However, considering the tests performed to satellites, the most destructive environmental tests are vibration and shock. During launch, satellites are exposed to severe vibration and shock loads transferred from the rocket (Araújo, 2024). These dynamic effects can cause structural damage which can lead to performance losses and catastrophic fails in the satellite components. Additionally, accurately predicting the dynamic behaviour of satellites during launch is crucial for both mission reliability and maintaining structural integrity. Therefore, it is important to determine the natural frequencies accurately in the CubeSat's dynamic analysis. In virtue of this fact, one of the most critical parameters is the applied boundary condition in determining the natural frequencies of CubeSats (Thimmaraju Girijadevi, 2023; Torres, 2024). Moreover, different boundary conditions can cause significant differences, especially in low-frequency modes, which leads to deviations in the analysis results from the actual system behaviour. In the literature, boundary conditions are commonly defined by three different approaches in CubeSat modal analyses. In the first approach, the CubeSat is analysed only with the bottom surface fixation boundary condition to simulate the worst case (García-López et al., 2019; Herrera-Arroyave et al., 2016). This approach leads to overdesigned structures. In the second approach, the CubeSat is analysed with a fixed boundary condition on both the bottom and top surfaces (Bostan et al., 2024; Elshaal et al., 2024). Here, since the connection is assumed to be rigid, the natural frequency is higher than the reality. In this case, there is a possibility that the actual frequency at low frequencies can be lower than the desired minimum frequency. In the third approach, the CubeSat's rails are fixed (Ampatzoglou & Kostopoulos, 2018; Kaya, 2019). Since this boundary condition exhibits stiffer behaviour compared to the second approach, the natural frequency results deviate more from the actual system behaviour.

In this study, an alternative boundary condition approach is proposed to realistically reflect the contact conditions at the CubeSat-pod interface. Additionally, it is aimed to accomplish more accurate dynamic effects that arise during launch, as opposed to the boundary conditions commonly used in the literature. In the proposed boundary condition, the CubeSat-pod interface contact was modelled as a spring. The contact stiffnesses between the CubeSat and the pod were calculated using the contact theories of Hertz, Mindlin, and Popov. By modelling these stiffnesses as spring elements, it was observed that the analysis results closely matched the test results with high accuracy. Furthermore, a minimum of 10% improvement was observed in the determination of natural frequencies when the proposed method was compared with boundary conditions commonly used in the literature.

2. Methodology

The first aim is to ensure the accuracy of the CubeSat's structural model in order to correctly model the CubeSat-pod interface (Wan Aasim et al., 2022). In this context, the modelling approach is based on the part-to-whole verification principle. The study is designed as a three-stage verification process.

In the first stage, a setup consisting solely of the printed circuit board (PCB) and standoffs was established. A sine sweep test was performed on the shaker to determine the system's natural frequency, and data was collected on the PCB by using accelerometer. A finite element (FE) model of the same system was created, and the diameter of the connection surface at the standoff-PCB interface was optimized to match the experimentally identified natural frequencies. Specifically, the interfaces were modelled using RBE3 elements that distribute the forces from the bolt head/nut to a circular region on the PCB. The only parameter adjusted during optimization was the diameter of this force-distribution region (D_{opt}). D_{opt} was iteratively modified in the range 5-7 mm until the first experimental natural frequency was reproduced within ±2%. In the second stage, a dummy mass was included in the model to create a PCB-standoff-dummy mass combination; this structure was also tested in a similar manner, and the natural frequencies of the system were determined. As in the first stage, an FE model was created, and the FE model was verified through analysis by optimizing the diameter of the connection surface at the dummy mass-PCB interface to match the experimentally identified natural frequencies. The same type of RBE3 connection was used at the dummy mass-PCB interface and D_{opt} was again tuned in the range 5-7 mm. No other parameters (bolt preload, material properties or element size) were changed during this optimization.

Once both interface parameters were fixed, they were kept constant in the full CubeSat model (Stage 3) without further adjustment. This approach ensures repeatability. The created FE model was analysed using boundary conditions commonly used in the literature and proposed in this study, and the natural frequencies obtained in each analysis were recorded. Following the analysis, the CubeSat model (Figure 1a) was created by bringing all components together. This model was placed inside the test pod (Figure 1b) and sine sweep tests were performed. The natural frequencies of the system obtained as a result of the tests were compared with the natural frequencies obtained as a result of FE analyses performed under the boundary conditions commonly used in the literature and proposed in this study.

The vibration tests were applied along three orthogonal axes with using a Dongling ES-100LS3-550 shaker system. The VR9500 controller and VibrationView 2017 software were utilized for system control and data acquisition. A Dytran 3055D2 single-axis accelerometer was employed for shaker control and data collection on the Test Pod, while a Dytran 3023A tri-axial accelerometer was used for data acquisition on the device under test (DUT).

The sine sweep test was conducted using a controlled sine sweep excitation. The frequency range was selected as 20–2000 Hz to cover the dominant local and substructure modes identified in the numerical analyses. The sweep was performed at a constant rate of 2 octaves per minute, and the excitation level was controlled at 1g to ensure linear system response and to avoid nonlinear effects during resonance crossings.

The test was carried out under closed-loop acceleration control at the shaker table, with appropriate limit settings applied to prevent excessive responses at resonance frequencies. The CubeSat–Pod assembly was mounted to the shaker using a dedicated fixture designed to provide repeatable boundary conditions and minimize parasitic stiffness effects. Resonance frequencies were identified from the frequency-domain acceleration responses by detecting peaks in the magnitude spectra across measurement locations.

All FE models were developed using Siemens NX 11.0 software, and NX Nastran was adopted as the solver. First, normal modes were extracted using SOL103 Response Dynamics solution type to obtain natural frequencies and mode shapes up to 2000 Hz. Subsequently, frequency response analyses representing the sine sweep base excitation were performed using the Modal Frequency Response method (still within the SOL103 Response Dynamics environment in NX). In this second step, a constant modal damping ratio of 2% was defined for all extracted modes. This value is a typical value used in aerospace qualification testing when no measured damping data are available and is considered conservative for lightly damped metallic and composite structures. The sine sweep event was simulated by applying a swept-sine base acceleration load (1g from 20 Hz to 2000 Hz) in each orthogonal direction, and acceleration responses were computed at critical locations.

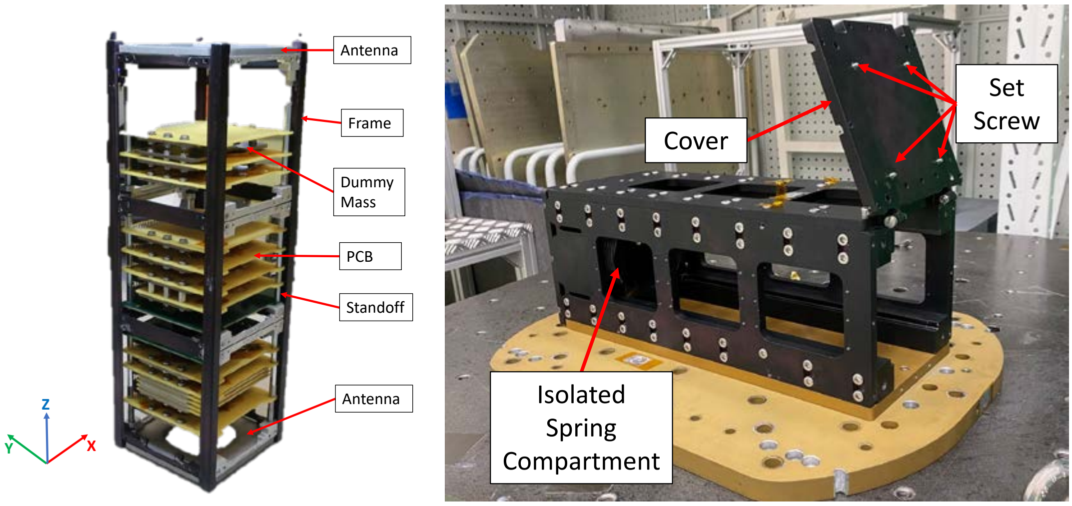

(a) **(b)**

Figure 1. (a) CubeSat and (b) Test pod.

2.1. PCB and Standoff Model Verification

In the first stage, a simplified test setup representing the CubeSat's components was created. As seen in Figure 2a, this setup consisted of one PCB and four standoff elements. The standoffs were attached to the fixture, and the PCB was secured to the standoffs at its four corners. Since the standoffs were made of aluminium, they were torqued to 0.5 Nm. An accelerometer was placed at the centre point of the PCB. The mechanical properties of the PCB and standoffs are given in Table 1.

Table 1. Mechanical properties of components.

Mechanical Properties	PCB	Standoff	Dummy Mass	Antenna	Frame
Material	Arlon 85N	Aluminium 6061	Stainless Steel	Aluminium 6061	Aluminium 6061
Density (g/cm^3)	1.6	2.70	7.8	2.70	2.70
Young’s Modulus (GPa)	24.8	68	200	68	68
Poisson’s Ratio	0.18	0.33	0.3	0.33	0.33

In the FE model (Figure 2b), the PCB was represented by 2D Shell elements, while the standoffs were represented by 1D CBEAM elements. Although the standoffs have a hexagonal cross-sectional area, they were modelled as 5.5 mm diameter circles with approximately equivalent cross-sectional area for simplicity. To justify this simplification, the equivalent circular cross-section was derived by matching the cross-sectional area (A), moments of inertia (I), and polar moment of inertia (J) of the original hexagonal standoff. A comparison of these properties is provided in Table 2, showing a maximum deviation of 2.5%, which is considered acceptable for global modal analysis.

Table 2. Cross sectional properties comparison.

Cross Sectional Properties	Hexagonal Cross Section	Circular Cross Section	Difference
Area, A (mm^2)	23.38	23.76	1.6%
Moment of Inertia, I (mm^4)	43.84	44.92	2.5%
Polar Moment of Inertia, J (mm^4)	87.69	89.84	2.5%

The standoff-PCB connection was implemented using RBE3 elements. The optimized connection surface on the PCB is a circle with a diameter of 5.5 mm. The accelerometer and cable weight were added to the model as a concentrated mass. Detailed information is given in the Table 3.

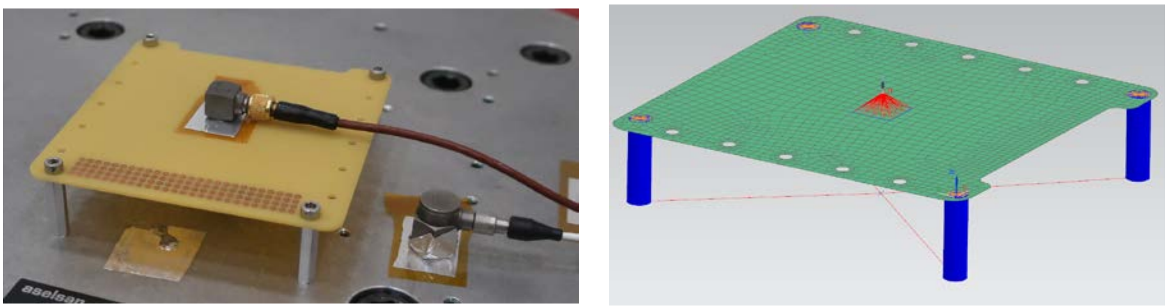

(a) **(b)**

Figure 2. PCB - standoff model (a) test setup and (b) FE model.

Table 3. FE model details of CubeSat.

Modelled Parts	Type of Mesh	Element Type
PCB	2D	CQUAD4
Standoff	1D	CBEAM
Dummy Mass	2D	CQUAD4
Antenna	3D	CHEXA8
Frame	3D	CHEXA8
Accelerometer	0D	CONM2
Connection Elements	1D	RBE2
Screw Head and Nut	1D	RBE3
Screw Threads	1D	CBEAM

2.2. PCB, Dummy Mass, and Standoff Model Verification

Following the first verification, a dummy mass, which is simulating the mass effects of electronic components, was mounted to the PCB (Figure 3a). The mechanical properties of the dummy mass are given in the Table 1.

The dummy mass was also modelled as a 2D Shell element; the six M3 screws connecting the dummy mass to the PCB were represented by 1D CBEAM elements for the threaded sections and RBE3 elements for the head and nut sections. The optimized connection surface between the dummy mass and the PCB is a circle with a diameter of 5 mm. Figure 3b shows the FE model. Detailed information is given in Table 3.

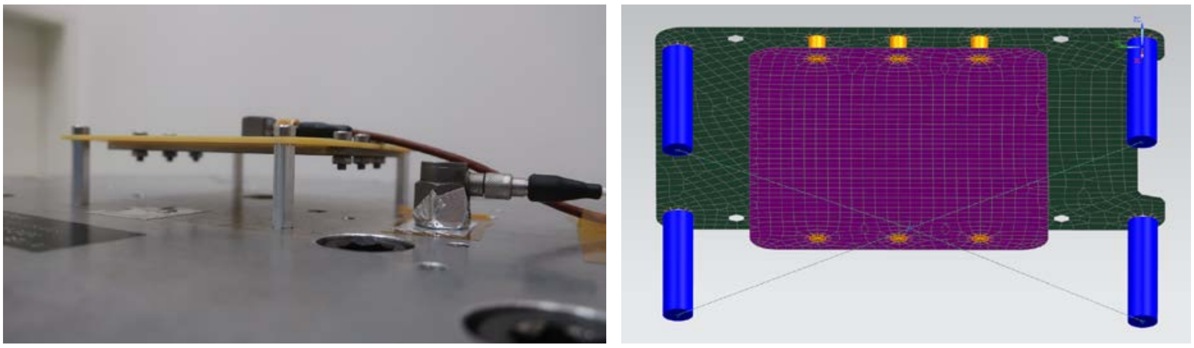

(a) **(b)**

Figure 3. PCB - dummy mass - standoff model (a) test setup and (b) FE model.

2.3. CubeSat Model Verification

As seen in the Figure 4, The CubeSat was modelled as a whole based on the information obtained during the verification of the FE models and connection interfaces of the PCB, dummy mass, and standoffs. A simplified structural CubeSat (Figure 1a) model was used for ease of processing. In the FE model, the CubeSat's frame and antennas were modelled by 3D elements, the PCBs and dummy masses by 2D Shell elements, and the standoffs by 1D elements. The PC104 connectors between the PCBs were modelled with RBE2 elements to reflect the rigid connection characteristic. Detailed information was given in Table 3.

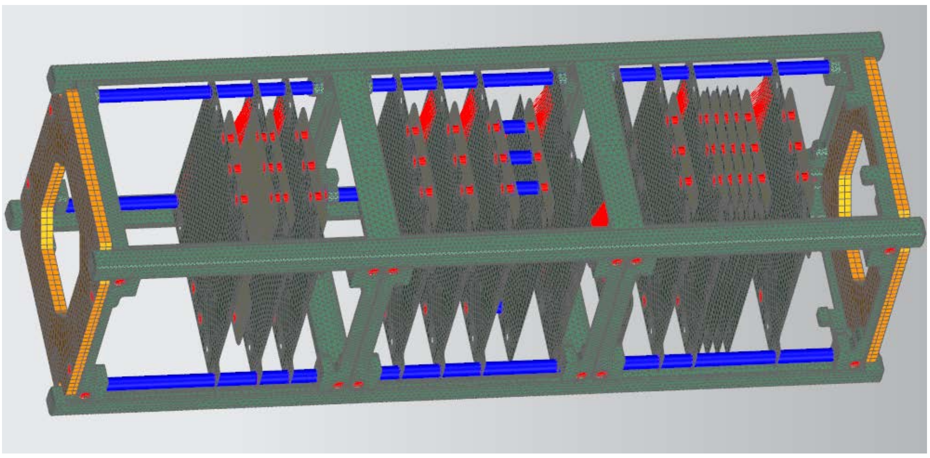

Figure 4. CubeSat FE model.

The three boundary conditions commonly used in the literature and the proposed boundary condition were applied to the FE models as described below, and dynamic analyses were performed.

Bottom fixation boundary condition (Figure 5a) is typically used in worst-case analyses. It is preferred when a cautious approach is adopted, as it yields lower natural frequencies compared to the real situation. During modelling, the four surfaces of the CubeSat's frame structure in the Z-axis direction were connected to the forced motion location point via RBE2 elements.

Top-bottom fixation boundary condition (Figure 5b) represents the situation where the CubeSat was squeezed by both the cover and the isolated spring compartment of the pod. However, fixing both surfaces increases the rigidity of the system and consequently causes the natural frequencies to be higher than in reality. In this case, the frame's total of eight surfaces in the -Z and +Z directions were connected to the enforced motion location point via RBE2 elements.

Rail fixation boundary condition (Figure 5c) simulates the situation where the CubeSat is held by the pod rails. However, this approach also causes the system to behave more rigidly than expected. During modelling, a total of eight surfaces of the frame along the lateral axis (X, Y) directions were connected to the enforced motion location point via RBE2 elements.

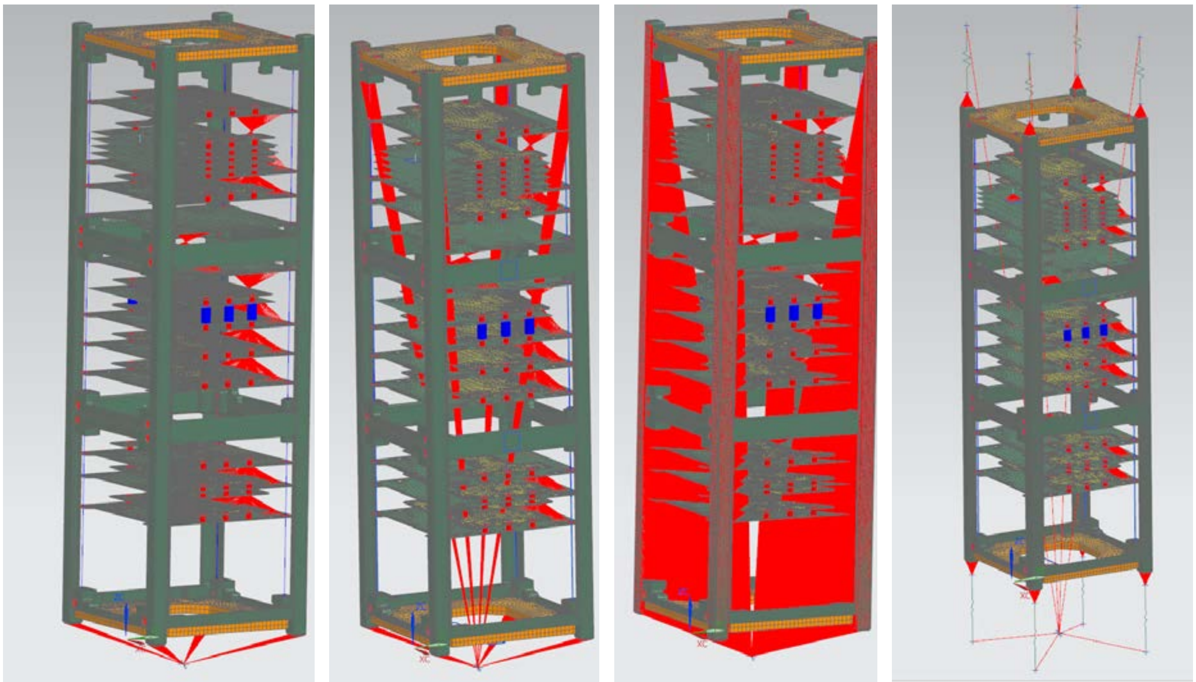

(a) (b) (c) (d)

Figure 5. Boundary conditions of (a) Bottom fixation, (b) Bottom-top fixation, (c) Rail fixation and (d) Proposed.

Proposed boundary condition (Figure 5d) is to model the contact between the bottom (-Z) and top (+Z) surfaces of the CubeSat Frame and the pod as a six-degree-of-freedom (6DOF) spring to reflect reality more accurately. The nominal distance between the rails of the test pod was measured as 100.3 ± 0.05 mm, while the distance between the CubeSat's rails was measured as 100 ± 0.1 mm, indicating an initial geometric clearance between the interfaces. Although these geometric tolerances indicate an initial clearance, localized contact under preload conditions introduced by the cover tightening cannot be completely excluded. To evaluate this possibility, post-test visual inspections of the CubeSat rail surfaces were conducted following the vibration tests. No evidence of wear, scratching, polishing, or material transfer was observed on the rail surfaces (Figure 6), indicating that any potential interaction was not sustained or rigid, but rather intermittent and compliant in nature. Therefore, the CubeSat was held under a certain pre-compression force by the cover and isolated spring compartment. However, this compression is not as rigid as the top-bottom fixation boundary conditions. Accordingly, the interface behaviour is more appropriately represented by a compliant six-degree-of-freedom (6DOF) spring boundary condition rather than an idealized fixed contact assumption.

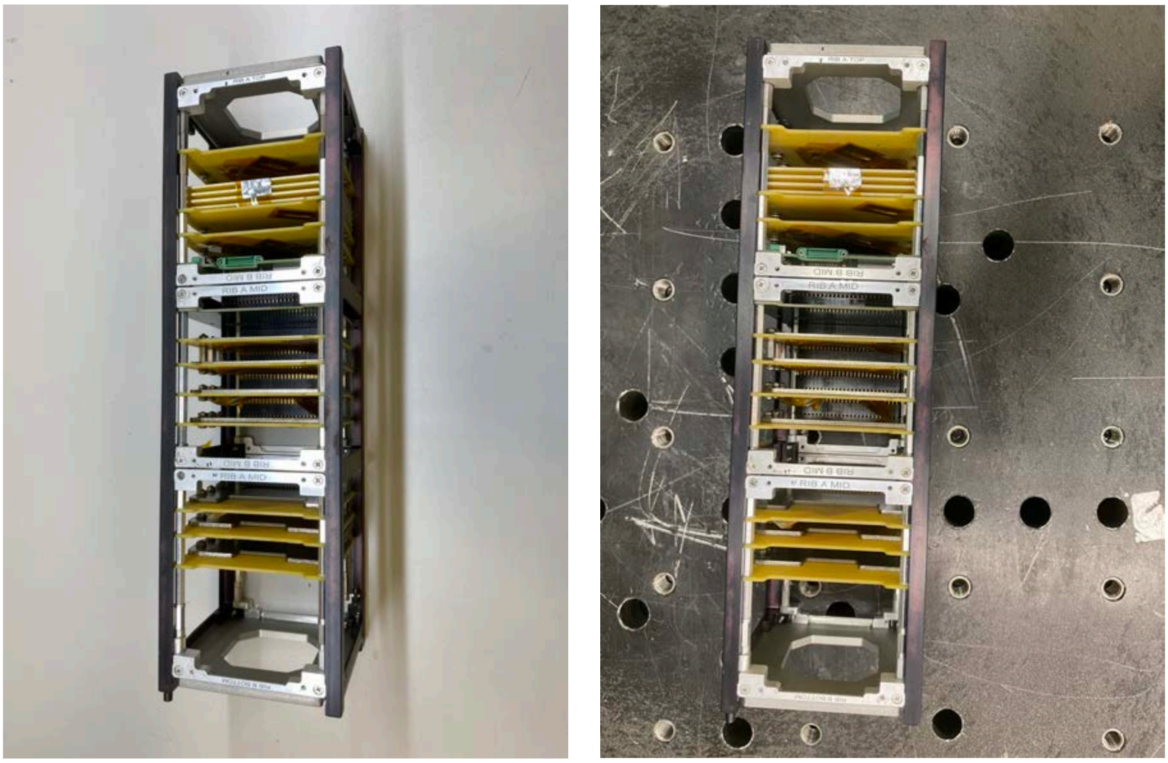

(a) **(b)**

Figure 6. CubeSat rails (a) Before and (b) After vibration test.

In the FE model, the aluminium frame-aluminium isolated spring compartment contact for the bottom end of the frame and the steel screw-aluminium frame contact for the top end were considered, and the stiffness values for these contacts were calculated using contact theory. After that, the CBUSH elements defined by the obtained stiffness values were connected to a total of eight surfaces in the bottom and top directions of the frame. The CBUSH elements were connected to these surfaces via RBE2 elements in order to distribute the contact stiffness over the interface region; the other ends of the CBUSH elements were also connected at the enforced motion location point using RBE2 elements. All six degrees of freedom of the

CBUSH elements were activated, including three translational (k_x, k_y, k_z) and three rotational stiffness components ($k_{\theta x}$, $k_{\theta y}$, $k_{\theta z}$), while no coupling terms between translational and rotational degrees of freedom were introduced. It should be noted that, the use of RBE2 elements may locally suppress rotational flexibility and slightly increase the effective interface stiffness, this modelling choice was intentionally adopted as a linearized and repeatable representation of the contact region, and its influence is considered acceptable for the global modal characteristics and frequency range investigated in this study.

After the different boundary conditions were defined for the model, the analyses were performed for each boundary condition. To enable a direct comparison between numerical and experimental results, analysis sensors were defined at the same locations as the accelerometers used during the sine sweep tests. The sensor has been defined to the frame along the lateral axis analyses and to the battery board along the longitudinal axis analyses on the CubeSat in order to be able to compare analysis and test results. Because the frame's natural frequency was higher than the test pod's natural frequency along longitudinal axis.

Following the analyses, a test setup was created to determine the CubeSat's natural frequencies in real conditions. The CubeSat under test has a structure consisting of a frame, dummy masses, and PCBs. This CubeSat was placed inside the test pod and subjected to a sine sweep test. After closing the pod cover, the M4 compression screws on it were tightened to a torque of 1.0 Nm each. This process was performed to prevent any possible movement of the CubeSat inside the pod. Test setups can be seen for each orthogonal axes in Figure 7.

To monitor dynamic behaviour, accelerometers were placed on both the CubeSat frame and the test pod. Additionally, an accelerometer was placed on the battery board along the longitudinal axis. Thus, the vibration responses of both the CubeSat and the pod were recorded simultaneously during the test.

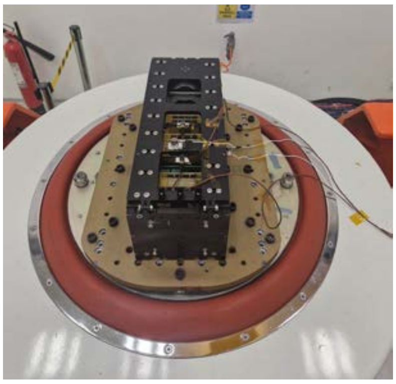
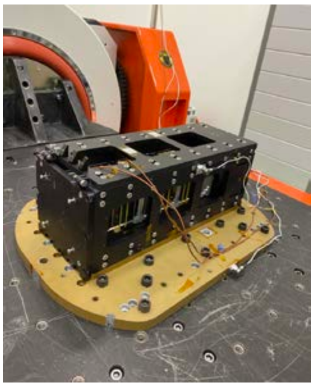
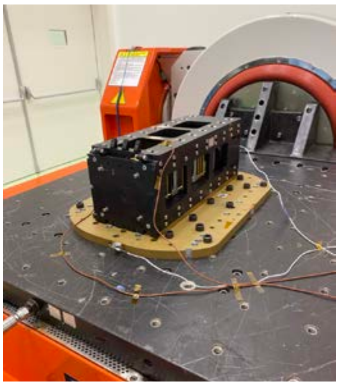

(a) **(b)** **(c)**

Figure 7. CubeSat vibration test setup in (a) X-axis, (b) Y-axis and (c) Z-axis.

2.4. Contact Theory

The classical framework describing the contact between two surfaces is the Hertz-Mindlin-Popov formulation (Popov, 2010). Hertz theory combines the elastic compliance of two halfspaces to give axial contact behaviour; Mindlin (and Cattaneo-Mindlin extensions) addresses tangential behaviour and partial/full stick-slip boundaries; Popov's axisymmetric solutions provide axial, tangential, and rotational contact stiffness in closed-form expressions, particularly for circular geometry (Popov, 2010).

The fundamental assumptions of the contact model are explicitly as follows: materials are isotropic, linear-elastic, and homogeneous; contact is smooth and adhesion/plastic deformation effects are neglected; deformations are small (small strains/rotations) and linear relations hold; geometry is assumed to be circular contact. Popov's axisymmetric flat punch results are directly applicable (Popov, 2010). Although the actual CubeSat–pod interface does not strictly conform to an ideal flat punch or perfectly circular geometry, the contact region remains small relative to the global structural dimensions and operates under high preload with limited local deformation. In this study, the contact formulation is employed to derive effective, linearized interface stiffness values for global dynamic modelling rather than to capture local stress concentrations or edge effects. Consequently, deviations from ideal geometry, surface roughness, and local edge effects are considered second-order influences on the global modal characteristics investigated.

Axial stiffness is calculated using the Equation (1) provided in Popov's solution for the axisymmetric flat punch.

$$k_z = 2E^* a \tag{1}$$

Where k_z depicts axial stiffness (N/mm), E* depicts Equivalent Young's modulus (MPa), a depicts contact radius (mm).

The equivalent elasticity modulus is a quantity specific to the material properties of the contacting surfaces (Popov, 2010).

When two surfaces are made of the same material, E*can be calculated according to Hertz's contact theory as shown in Equation (2):

$$\frac{1}{E^*} = \frac{2(1 - v^2)}{E} \tag{2}$$

Where E depicts Young's modulus (MPa), v depicts Poisson's ratio.

When the two surfaces are made of different materials, E* can be calculated according to Hertz's contact theory as given in Equation (3):

$$\frac{1}{E^*} = \frac{1 - v_1^2}{E_1} + \frac{1 - v_2^2}{E_2} \tag{3}$$

Tangential stiffness is calculated using the Equation (4) given in Popov's solution for an axisymmetric flat punch.

$$k_x = k_y = 2G^* a \quad (4)$$

Where k_x, k_y depicts tangential stiffness (N/mm), G* depicts equivalent shear modulus (MPa), a depicts contact radius (mm)

The equivalent shear modulus G* used in the tangential stiffness calculation is given by the following Equation (5):

$$\frac{1}{G^*} = \frac{2 - v_1}{4G_1} + \frac{1 - v_2}{4G_2} \quad (5)$$

Where G_i depicts i^{th} of shear modulus.

The shear modulus is calculated using Poisson's ratio and Young's modulus from the Equation (6):

$$G_i = \frac{E_i}{2(1 + v_i)} \quad (6)$$

The linear coefficients directly used from Popov's axisymmetric flat-punch and related rotation/torsion solutions are shown in Equation (7) and Equation (8):

$$k_{\theta_z} = \frac{16}{3} G^* a^3 \quad (7)$$

$$k_{\theta_x} = k_{\theta_y} \approx \frac{8}{3} E^* a^3 \quad (8)$$

Where k_{θ_x}, k_{θ_y} depicts bending stiffness, k_{θ_z}depicts torsional stiffness.

The aluminium square-section frame on the bottom of the CubeSat contacts the aluminium isolated spring holder (Figure 8a). When the 6x6 mm² square contact area of the frame was converted to an equivalent circular radius, the value a was calculated as 3.38 mm. Considering the calculated equivalent contact radius and aluminium-aluminium contact, the determined stiffness values are given in Table 4.

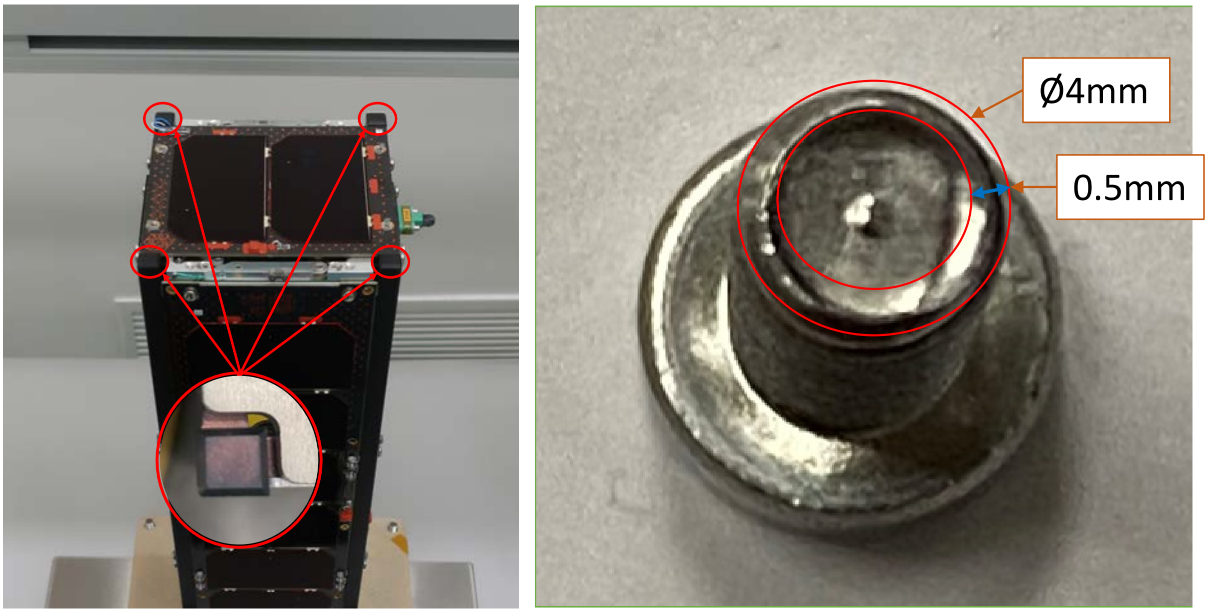

(a) **(b)**

Figure 8. Cross sectional image of (a) Frame contact surface, and (b) Screw.

The top of the CubeSat, the steel screw-aluminium frame contact used to compress the CubeSat was considered. Here, the outer surface of the screw's circular cross-section was in contact, as seen in Figure 8b. When the equivalent radius was calculated for this contact, the value a was found to be 1.32 mm. Considering the calculated equivalent contact radius and steel-aluminium contact, the determined stiffness values are given in Table 4.

Table 4. Contact stiffness value of CubeSat-pod interface.

Stiffness	Unit	Al-Al	SS-Al
Tangential Stiffness (k_x, k_y)	N/mm	2.1×10^5	1.2×10^5
Axial Stiffness (k_z)	N/mm	2.6×10^5	1.5×10^5
Bending Stiffness ($k_{\theta_x}, k_{\theta_y}$)	Nmm/rad	4.1×10^6	3.5×10^5
Torsional Stiffness (k_{θ_z})	Nmm/rad	6.5×10^6	5.7×10^5

Using the standard torque-tension approximation, torque preload is calculated from the Equation (9):

$$F = \frac{T}{K * d} \tag{9}$$

Where T depicts tightening torque, F depicts torque preload, K depicts torque coefficient, d depicts nominal diameter of screw.

The nominal bolt preload is calculated 1250 N from Equation (9) using these values.

T is 1.0 Nm, K is 0.2 (nominally 0.2-0.3), d is 4 mm (nominal diameter of M4), and deformation (δ_{max}) is calculated from Equation (10).

$$\delta_{max} = \frac{F}{k_z} \tag{10}$$

To assess an upper-bound deformation, the minimum normal contact stiffness used in the model (k_z=1.5×10^5 N/mm) was considered, resulting in a worst-case local deformation of approximately δ_{max}=8.3 μm. This small deformation magnitude supports the assumption of small, elastic contact deformation and justifies the use of a linearized contact stiffness representation around the nominal assembled condition.

3. Results and Discussion

The simulation results were verified with the sine sweep tests. In the first stage, the PCB and standoff setup was attached to the vibration test device perpendicular to the PCB's surface. According to the sine sweep test result, it was revealed that the PCB has 360 Hz of first natural frequency. Since the difference between the first natural frequencies was around 1.4%, the FE model created was found to be highly accurate. The analysis and test results are given in Figure 9. Subsequently, first natural frequency was simulated as 365 Hz in the modal analysis (Figure 11a).

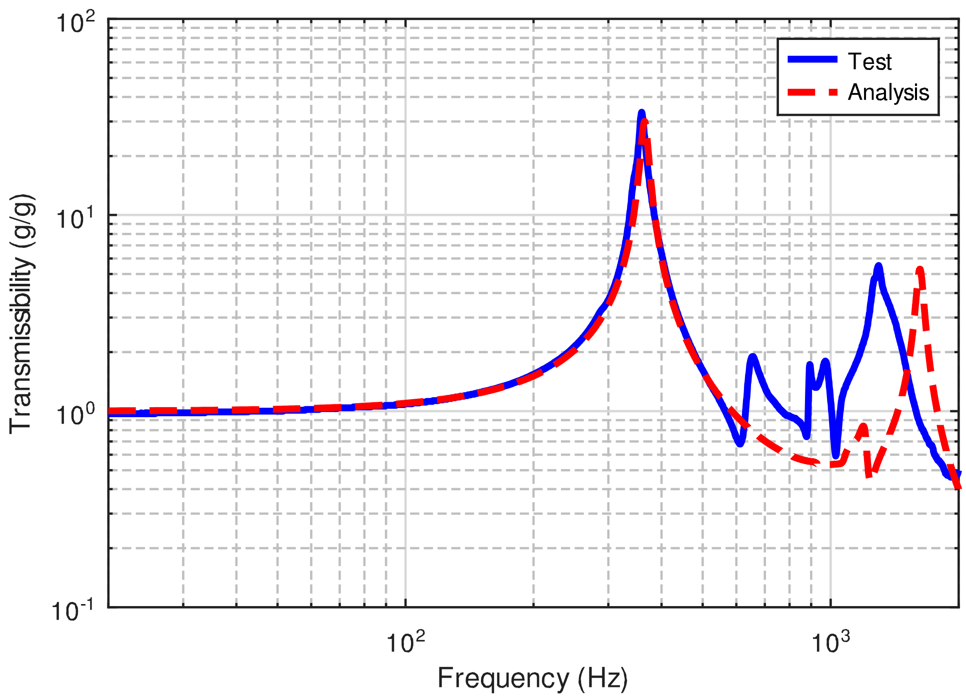

Figure 9. Test and analysis result of PCB-standoff setup.

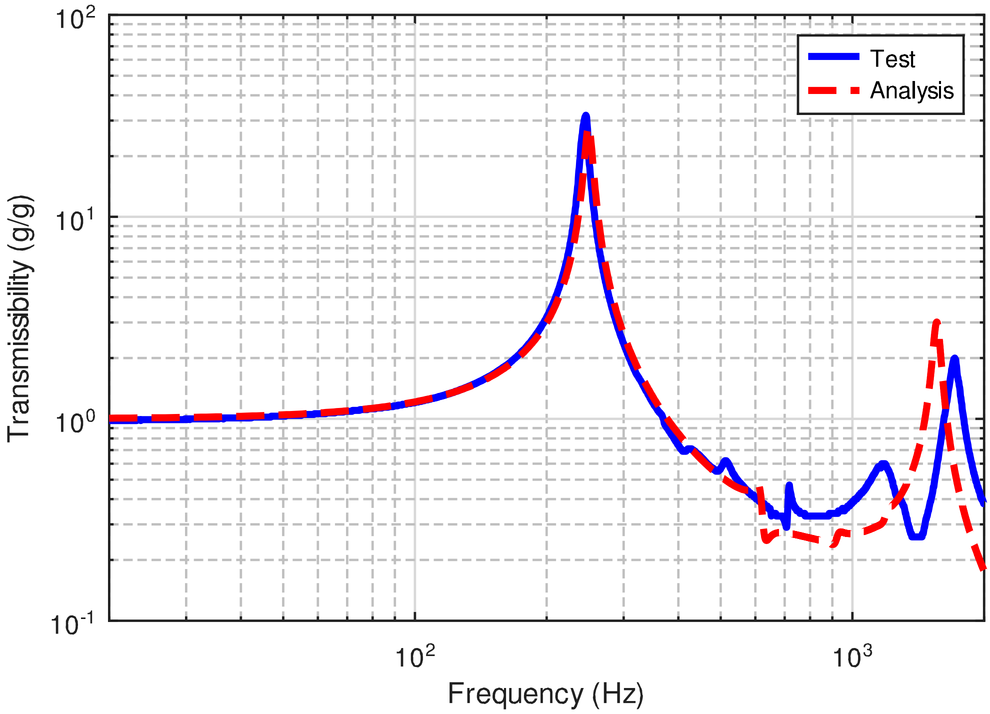

Figure 10. Test and analysis result of PCB-dummy-standoff setup.

Following this verification, a dummy mass was attached to the PCB-standoff setup in the first stage. According to the sine sweep test result, it was revealed that the setup has 246 Hz of first natural frequency. Since the difference between the first natural frequencies was around 1.6%, the created FE model was found to be highly accurate. The analysis and test results can be seen in Figure 10. Subsequently, first natural frequency was simulated as 250 Hz in the modal analysis (Figure 11b).

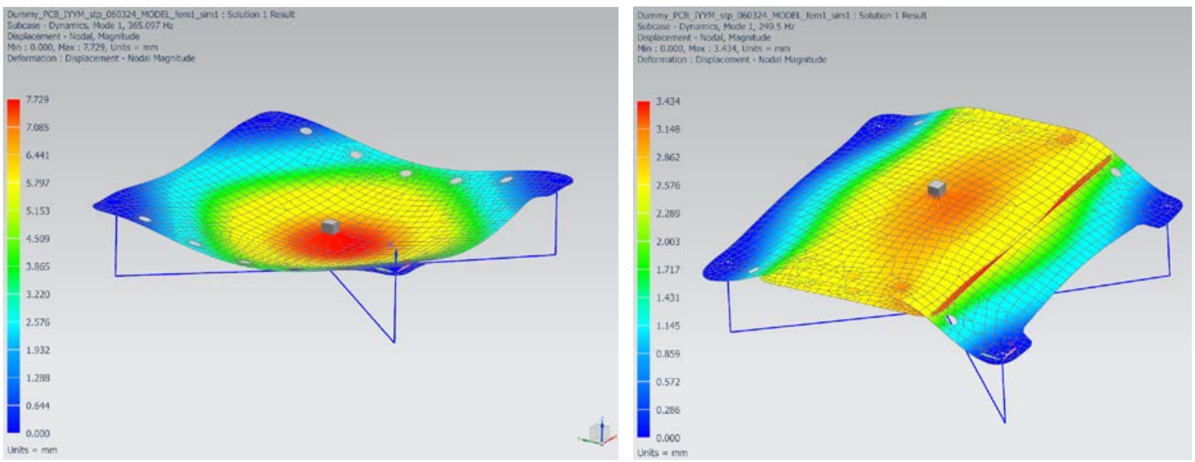

(a) (b)

Figure 11. First natural frequency and mode shape of (a) PCB-standoff, and (b) PCB-dummy mass-standoff.

Then, in Stage 3, the CubeSat was modelled based on the FE models verified in the previous stages. FE analyses were performed under three different boundary conditions found in the literature and the proposed boundary condition. First natural frequencies and mode shapes can be seen in Figure 12.

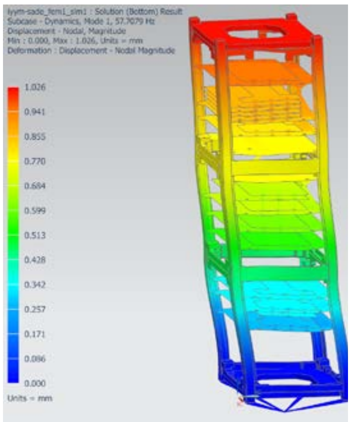

(a)

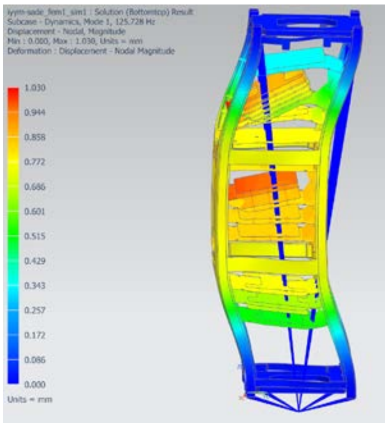

(b)

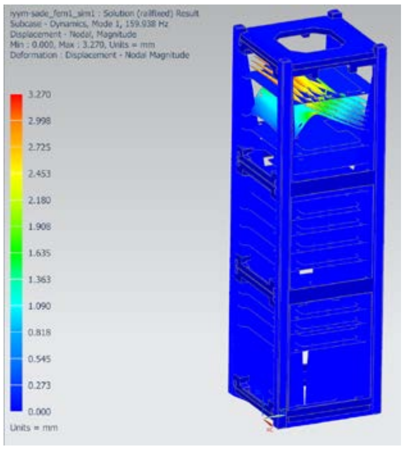

(c)

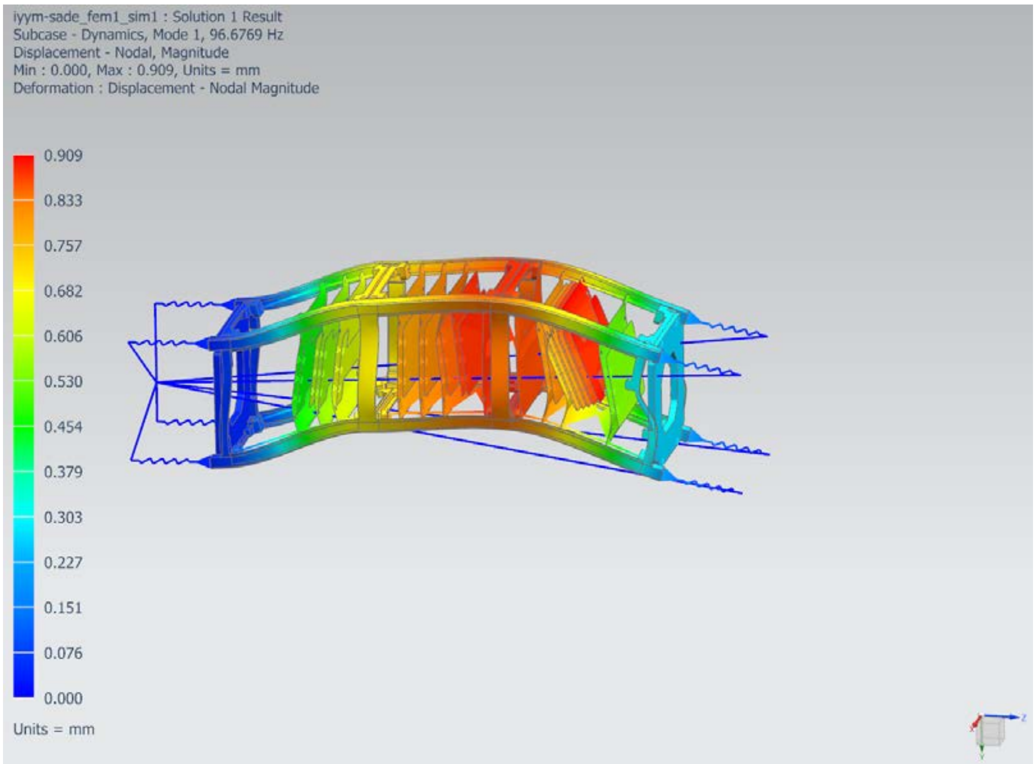

(d)

Figure 12. First natural frequencies for boundary conditions of (a) Bottom fixation, (b) Bottom-top fixation, (c) Rail fixation, and (d) Proposed.

Upon completion of the analyses, the CubeSat was mounted to the shaker in the test pod for 3 orthogonal axes. Sine sweep test was performed separately for all 3 axes. During the tests, the data were obtained from the frame along the lateral (X and Y) axes. As seen in the Figure 13 and Figure 14, the CubeSat frame shows clear resonance peaks that appear before the dominant pod modes, indicating that the frame natural frequencies are lower than those of the pod and can be distinguished from the test data. In contrast, along the longitudinal Z-axis, the pod and CubeSat frame show overlapping resonance behaviour in the frequency-domain acceleration responses, indicating strong dynamic coupling between them (Figure 15). This observation indicates that the global frame natural frequency in the longitudinal direction is higher than the corresponding pod mode and therefore cannot be clearly identified from frame-mounted measurements. Consistent with the analysis results, the first clearly identifiable mode along the Z-axis is associated with the battery board, which shows a distinct local resonance in both the analysis and the experimental data. For this reason, the battery board mode was selected as the representative first longitudinal mode, and the comparison between analysis and test results was performed using acceleration data measured on the battery board.

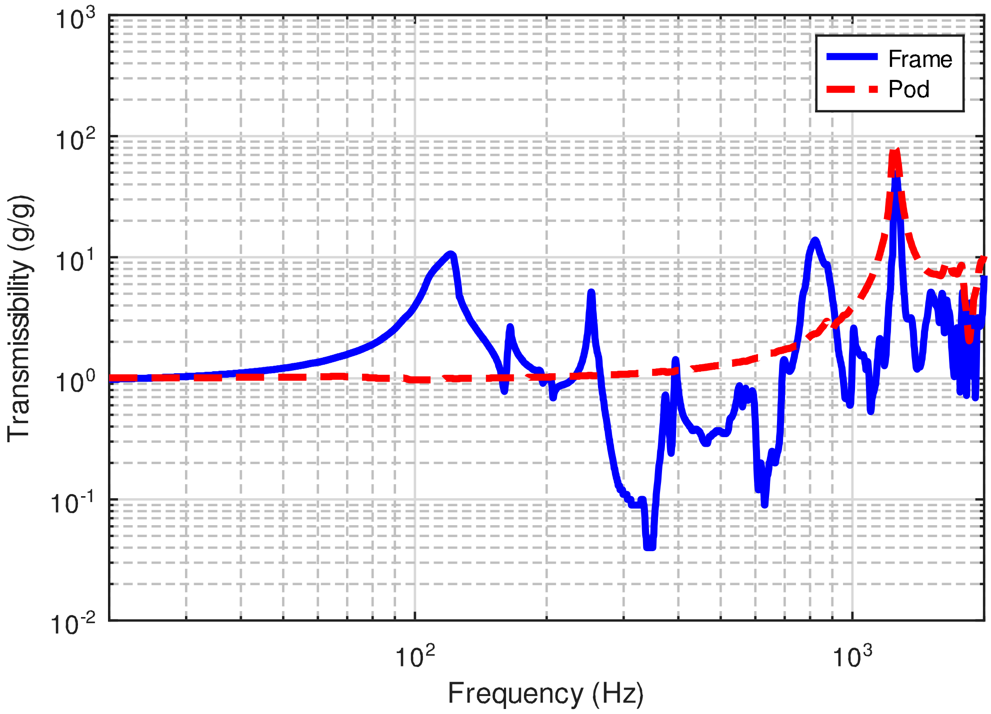

Figure 13. Test result of CubeSat and pod along X-axis.

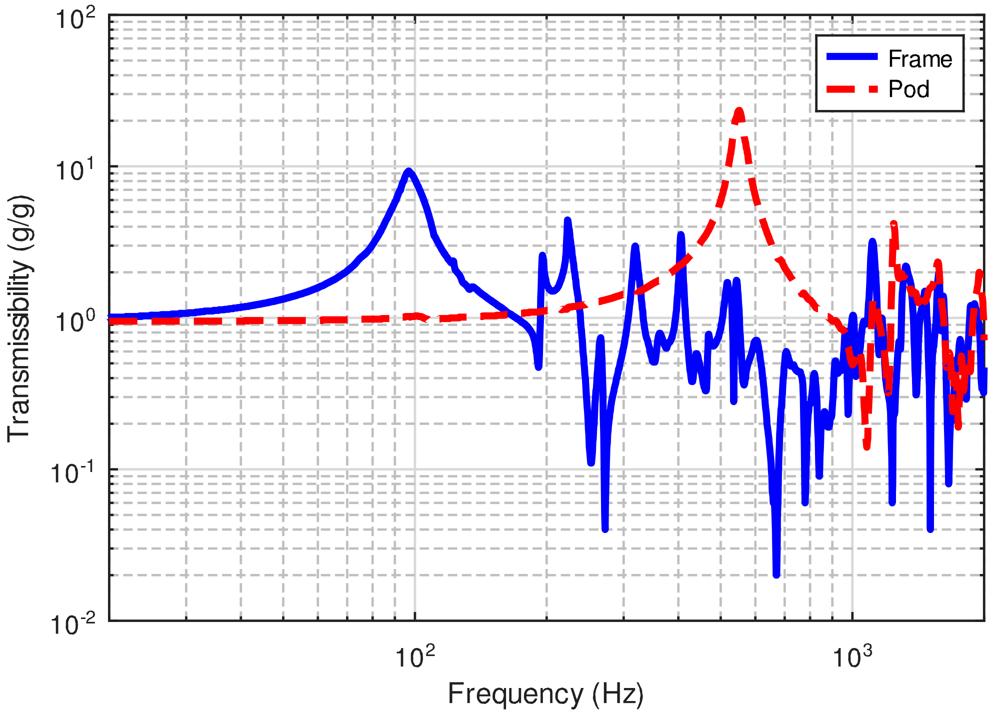

Figure 14. Test result of CubeSat and pod along Y-axis.

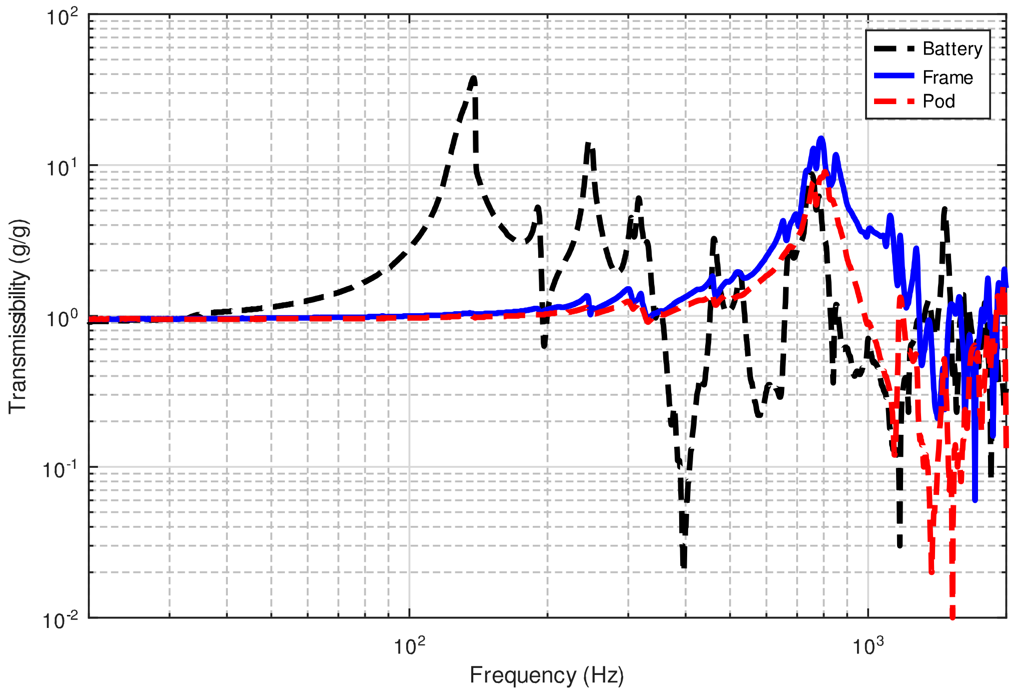

Figure 15. Test result of CubeSat and pod along Z-axis.

As seen in the Figure 16, Figure 17, and Figure 18 the results of the analyses, which were performed with different boundary conditions, were compared with the test results. Along the lateral (X and Y) axes, it was observed that the natural frequencies were lower than expected when fixed at the bottom end, and higher when fixed at both the bottom and top ends. In the case of being fixed to the rails, the natural frequency along the lateral axes was not included in the calculation. Since no dominant global frame mode was observed up to 2000 Hz and the response is governed by local PCB and standoff modes, quantitative comparison among boundary conditions primarily affecting the frame behaviour is not physically meaningful within the investigated frequency range.

Along the longitudinal axis, since the first natural frequency was on the battery board, the boundary conditions used in the literature were similar. However, they differed by minimum 15% from the actual test result. On the other hand, the test and simulation results were similar for the proposed boundary conditions.

When the test results and analyses results performed with the proposed boundary condition were compared, along the lateral axes, natural frequency values of 96 Hz and 126 Hz were obtained in the analysis, and 96.7 Hz and 120 Hz in the test, respectively (Figure 16 and Figure 17). Along the longitudinal axis, according to the results, it was observed that the lowest natural frequency was on the battery board. As a brief, a natural frequency of 137.9 Hz and 138 Hz respectively in the test and analysis (Figure 18).

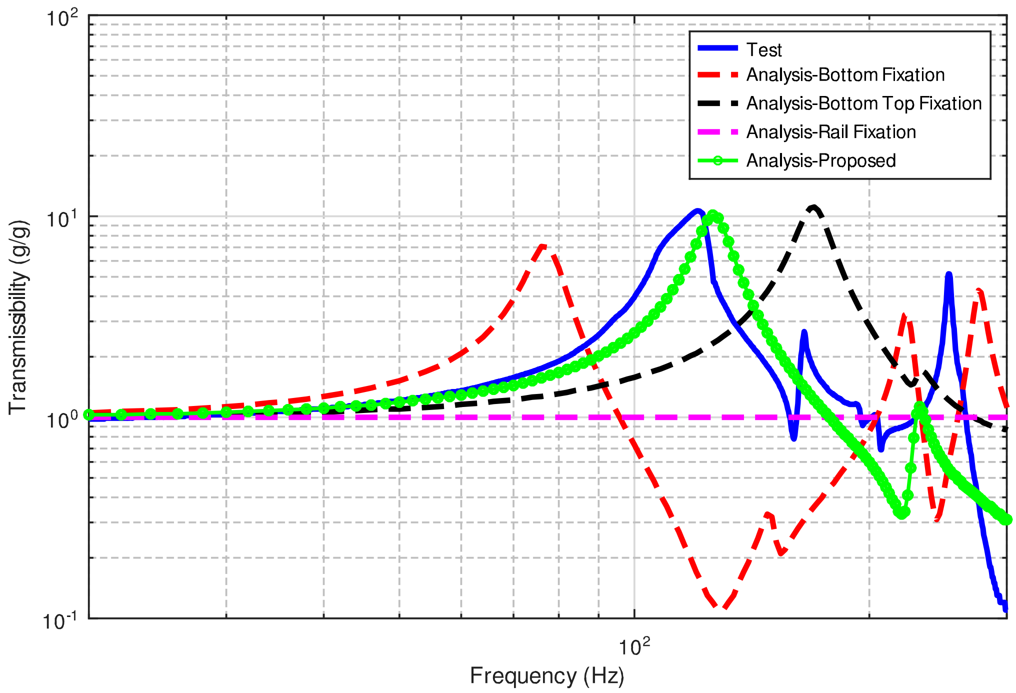

Figure 16. Test result and analysis results of different boundary conditions along X-axis.

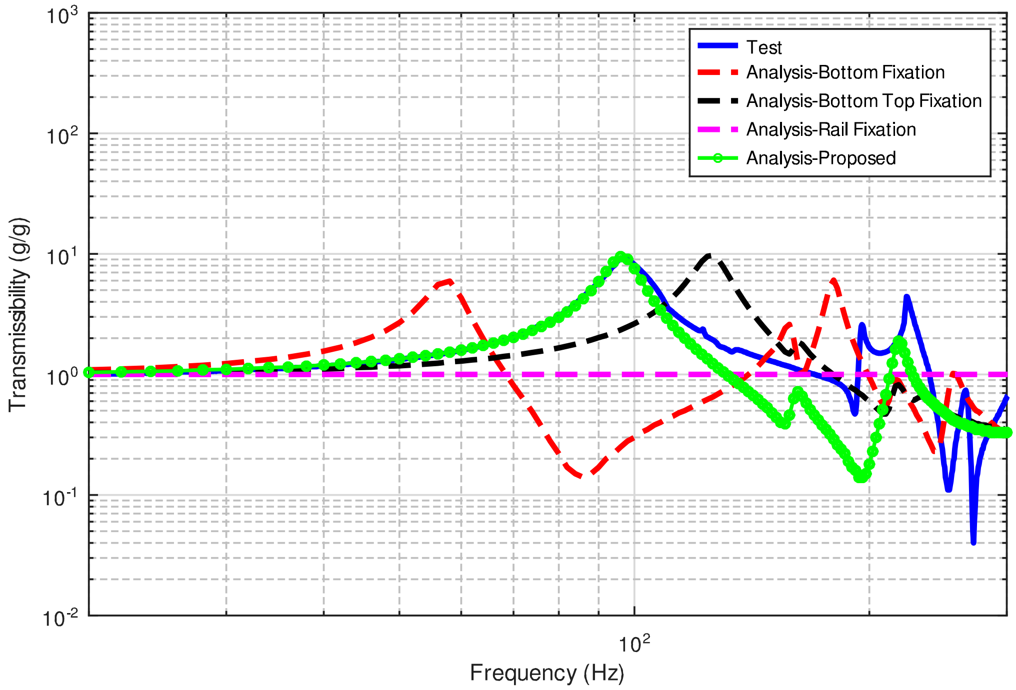

Figure 17. Test result and analysis results of different boundary conditions along Y-axis.

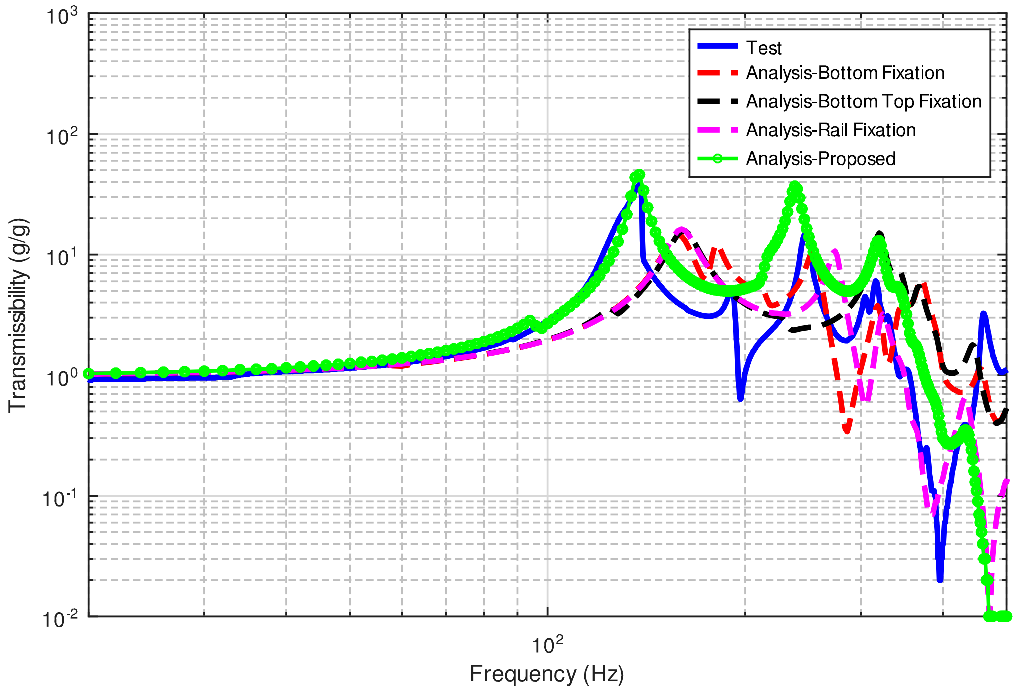

Figure 18. Test result and analysis results of different boundary conditions along Z-axis.

Mode matching between numerical and experimental results was performed based on a combined evaluation of frequency proximity, excitation direction, and dominant deformation characteristics observed in the numerical mode shapes. In addition to frequency agreement, the physical interpretation of the mode shapes obtained from the finite element analysis was used to ensure consistent mode pairing. To support this interpretation, the first lateral mode shapes obtained from the numerical analysis along the X and Y axes are presented in Figure 19 and Figure 20, corresponding to the 126 Hz and 96 Hz modes, respectively, which clearly demonstrate distinct and physically meaningful deformation patterns used for mode identification.

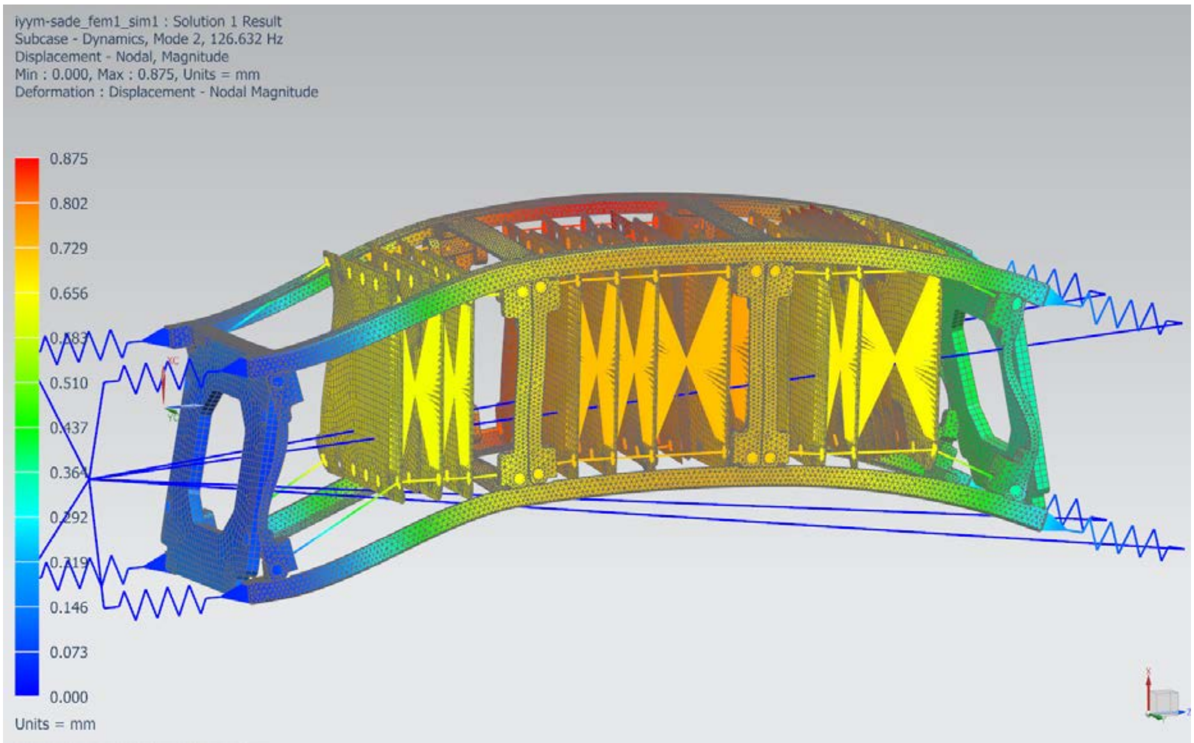

Figure 19. First natural frequency and mode shape along X-axis.

When the boundary condition cases adopted from the literature are compared with the experimental results, the smallest deviation is 14.7%, observed for the bottom-fixed configuration along the longitudinal Z-axis. This value represents the best-case agreement among the literature-based boundary conditions. For the proposed contact-based boundary condition, the maximum deviation is 4.7%, occurring along the lateral X-axis, which corresponds to the worst-case result of the proposed approach. Overall, the proposed method exhibits consistently smaller deviations from the experimental results compared to the literature-based boundary conditions, indicating improved agreement with the measured CubeSat–pod dynamic behaviour.

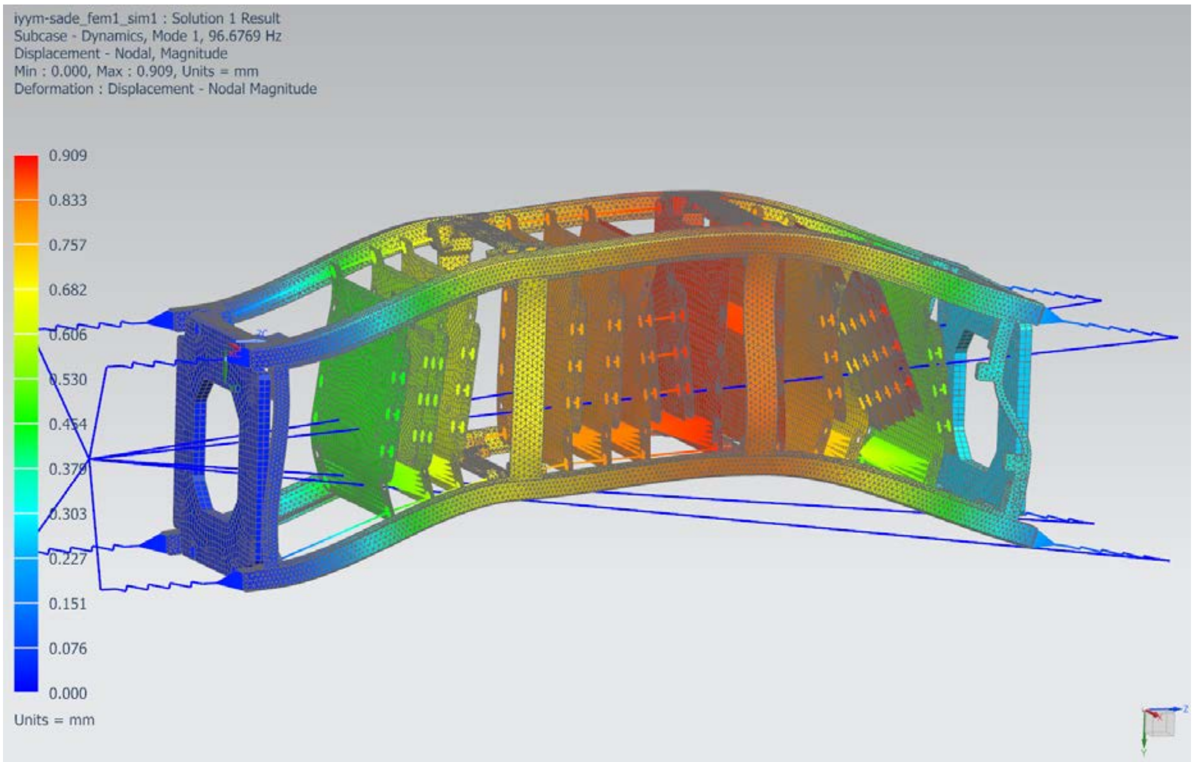

Figure 20. First natural frequency and mode shape along Y-axis.

These findings highlight the limitations of conventional boundary conditions commonly employed in CubeSat structural analyses. For example, the bottom fixation approach, as utilized by García-López et al. (2019) and Herrera-Arroyave et al. (2016), simulates a worst-case scenario but often results in overly conservative designs by underestimating the system's stiffness, leading to lower predicted natural frequencies and potential overdesign. Similarly, the bottom-top fixation, adopted in studies like Elshaal et al. (2024) and Bostan et al. (2024), assumes rigid connections that overestimate rigidity, yielding higher frequencies than observed in tests and risking optimistic predictions that could compromise mission reliability. The rail fixation method, seen in Ampatzoglou and Kostopoulos (2018) and Kaya (2019), further exacerbates this by imposing even stiffer constraints, deviating significantly from real pod interactions.

In contrast, our proposed contact-based boundary condition, derived from Hertz-Mindlin-Popov theories and modelled via 6DOF spring elements (CBUSH), captures the compliant nature of the CubeSat-pod interface more realistically. This approach accounts for preload-induced contacts and geometric clearances, which are often neglected in literature models. By incorporating contact stiffnesses, our method reduces deviations to a maximum of 4.7% (an enhancement of over 10% in prediction accuracy compared to these traditional approaches) demonstrating its originality in bridging the gap between FEA and real-world launch dynamics without requiring excessive computational complexity or empirical adjustments.

4. Conclusion

The findings revealed that the boundary conditions in the literature were insufficient to reflect the actual behaviour along the lateral axes. In contrast, the contact model proposed in this study -an approach using 6DOF spring elements (CBUSH) at the CubeSat-pod interface showed high alignment with the test data. As a result, the difference between analysis results from the proposed boundary condition modelling and the test results was found to be at maximum 4.7%, confirming that the model accurately represents the physical behaviour. This approach increases the reliability of structural-dynamic analyses, especially under launch conditions, and provides a more realistic modelling basis for CubeSat designs. The original contribution of this work lies in its departure from rigid or overly simplified boundary conditions prevalent in the literature, which often lead to either conservative overdesigns or risky underestimations of dynamic responses. Future studies may extend the proposed modelling approach to different launcher pod configurations since CubeSat-pod interface behaviour can vary with pod design. Some launcher pods use rail mechanisms that actively clamp the CubeSat, leading to sustained and preload-dependent rail contact in addition to the top-bottom interfaces considered in this study. For such cases, the modelling framework can be expanded to explicitly include rail contact and its stiffness effects. This extension would improve the applicability of the proposed approach to a wider range of launch environments.

Conflict of Interest

There is no conflict of interest among authors.

Author Contributions

Ulusoy E., and Öztürk S. were carried out this research and performed measurements. Ulusoy E., Öztürk S., and Arıcan G. O. were written the manuscript.

Funding

This research received no funding.

Acknowledgments

The authors are grateful to Aselsan Inc. for providing simulation production and measurement infrastructure.

Ethical Statements

Not applicable.

Data and Code Availability

Not applicable.

Supplementary Materials

Not applicable.

References

Ampatzoglou, A., & Kostopoulos, V. (2018). Design, analysis, optimization, manufacturing, and testing of a 2U CubeSat. *International Journal of Aerospace Engineering, 2018*, Article 9724263. https://doi.org/10.1155/2018/9724263

Araújo, L. (2024). *Dynamic Response of a CubeSat within a Deployer during Launch Phase.* MSc Thesis, IST Lisbon.

Areda, E. E., Cordova-Alarcon, J. R., Masui, H., & Cho, M. (2022). *Development of Innovative CubeSat Platform for Mass Production*. *Applied Sciences*, 12(18), 9087. https://doi.org/10.3390/app12189087

Bomani, B. M. M., et al. (2021). *CubeSat Technology Past and Present: Current State-of-the-Art*. NASA TP-20210000201.

Bostan, V., Guţu, M., Melnic, V., & Martîniuc, A. (2024). Structural analysis and vibration testing of the tumnanosat microsatellite. *Journal of Engineering Sciences*, (4), 8-21. https://doi.org/10.52326/jes.utm.2024.31(4).01

Elshaal, A., Okasha, M., Sulaeman, E., Jallad, A. H., Aizat, W. F. A., & Alzubaidi, A. B. (2024). Structural analysis of AlAinSat-1 CubeSat. *Egyptian Journal of Remote Sensing and Space Sciences*, *27*(3), 532–546. https://doi.org/10.1016/j.ejrs.2024.06.006

García-López, A., Sánchez, J., & Arévalo, L. (2019). Structural design and analysis of a 3U standardized CubeSat for a future Mexican mission. *In Proceedings of the XXXII Congreso de Instrumentación de la Sociedad Mexicana de Instrumentación (SOMI)*, Acapulco, México.

Herrera-Arroyave, J. E., Bermúdez-Reyes, B., Ferrer-Pérez, J. A., & Colín, A. (2016, September 26–30). CubeSat system structural design. *In Proceedings of the 67th International Astronautical Congress (IAC)* (pp. 1–5). Guadalajara, Mexico.

Kaya, A. (2019). *Kompozit 3U küp uyduların yapısal analizi ve tasarımları* (Yüksek lisans tezi, İstanbul Teknik Üniversitesi).

Kanavouras, K., Hein, A.M., & Sachidanand, M. (2022). *Agile Systems Engineering for sub-CubeSat scale spacecraft.* https://arxiv.org/pdf/2210.10653

Kempf, J., Mühlbauer, T., & Dasbach, H. (2021). *Space Factory 4.0 – Industry 4.0 approaches for automated small-satellite production*. In *Proceedings of the 72nd International Astronautical Congress (IAC 2021)*. International Astronautical Federation.

Popov, V. L. (2010). *Contact mechanics and friction: Physical principles and applications.* Springer.

Thimmaraju Girijadevi, L. (2023). *Vibration analysis and testing of a 6U CubeSat propulsion system*. MSc Thesis, KTH. https://www.diva-portal.org/smash/record.jsf?pid=diva2%3A1817018&dswid=-6733

Torres, A. E. i. (2024). *Manufacturing Process of a CubeSat Structure.* Master's thesis, Universitat Politècnica de Catalunya.

Wan Aasim, W. F. A., AlMazrouei, M., Okasha, M., & Jallad, A. H. (2022). The structural analysis of AlainSat-1: An earth observation 3U CubeSat. *In 4th Symposium on Space Educational Activities. Universitat Politècnica de Catalunya.*